Thermal measurements Chapter 4

4.1 Introduction

In this chapter, a thermal imaging camera with a microscopic lens is used to examine the front facet, top contact and back facet temperatures of the same series of devices measured in Chapter 3. Until now, little data has been available on the temperature changes in 1.3μm dilute nitride devices caused by self heating. By measuring the emission spectra over a wide range of heat sink temperatures and injection currents, the active region temperature is also determined. Comparatively small rises in both facet and QW temperature are observed at high injection currents.

4.2 Thermographic imagery

Thermographic imagery is a well known technique for the study of defect formation and device degradation. In a recent study [1], as a device was aged over 3000 hours a considerable increase in emission in both the near and mid IR was observed. The increase in mid-IR emission is associated with an increased device temperature. The increase in near-IR emission was attributed to mid-band-gap deep-level defect formation. Measurement systems have been developed with two optical channels [2], enabling deep level luminescence to be separated from other thermal effects [3]. Indeed, due to its high speed, thermography is highly attractive as a device screening technique [4]. Devices with hot-spots or large deep-level defect concentrations can be identified quickly during manufacture and discarded.

The thermal imaging technique lends its self to the quick evaluation of large areas, such as the front facet or top contact window. However, due to the relatively low spatial resolution of the thermal imaging technique (~30x30μm), it usual to use another technique [5] to determine the facet temperature around the active region. A variety of methods have been proposed in the literature for the detailed measurement of the front facet temperature:

- *Raman microprobe microscopy* [6] measures the Stokes/anti-Stokes phonon line intensity ratio [7]. The technique is very slow and only has an accuracy of ±20K. The excitation laser must be powerful and may cause additional facet heating [7].
- *Micro-photomodulated reflectance photoreflectance* [8] uses the dependence of facet reflectivity on temperature. The advantage of the technique is that it is rapid. However, this technique requires very accurate alignment of the probe laser [7].
- *Electro-luminescence* uses the light from the laser facet itself [7,9].

The high photon density and high surface recombination rates make the front facet the hottest part of a device. Indeed it is common for high powered laser diodes to fail due to the front facet being melted in catastrophic optical damage (COD). Thus, another technique is required to measure the active region temperature itself. Commonly, the magnitude of the red-shift of the emission spectra is used to determine the active region temperature [10].

Thermographic imagery has previously been used to investigate the thermal performance of a wide range of devices, including 808nm [5] and 650nm high-power broad-area devices [3]. As yet, however, no thermal measurements have been performed on the 1.3μm devices studied in Chapter 3. Understanding the thermal characteristics of these devices is of particular interest, because they are very temperature stable, but however, have relatively short lifetimes. Any knowledge that can be gleaned from thermal measurements and could be used to increase the lifetimes would be of great use in further developing the material system.

4.3 Thermography with a thermal camera

4.3.1 Experimental setup

The experimental set-up used to measure the thermal performance of the devices is shown in figure 4.1. The system is essentially the same as that used for the measurement of ASE spectra in Chapter 3. However, the fibre, computer controlled stage and OSA have been replaced with a *Flir SC3000* thermal imaging camera. The camera was positioned to look down on the device at 45^{o} to the front facet. This allows the top contact and the front facet to be imaged at the same time. Images from the camera were retrieved by computer and stored on disk. The camera has a sensitivity of 20mK, a spatial resolution of 30x30μm and detection wavelength between 7-9μm. This is achieved using a 320 x 240 pixels GaAs Quantum Well Infrared Photodetector (QWIP) cooled to 70K.

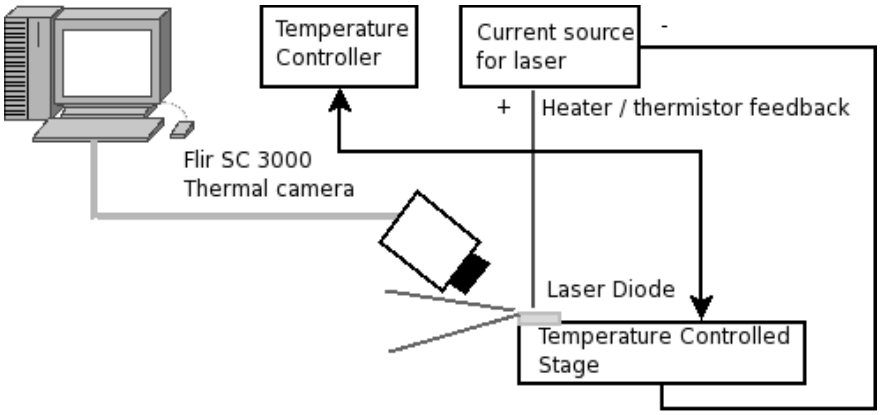

Figure 4.1: Experimental setup to perform thermal measurements.

The camera determines the temperature of an object by measuring the amount of radiation emitted between 7-9μm. All objects do not emit the same amount of radiation at a given temperature. Thus, the temperature values reported by the camera will not be true temperatures. The ratio of the amount of radiation emitted by a material at temperature T_1 to the amount of radiation emitted by a perfect black body at the same temperature T_1 is defined as the emissivity. The laser diode and sub-mount contain a wide range of materials of different emissivities. A list of these materials and their emissivities is given in table 4.1.

Use	Material	Emissivity	Reference
Submount	Cu	0.78	[11]
Contacts	Au	0.82	[11]
Substrate	GaAs	0.75	[12]
Laser Epitaxy	GaInAsN/GaAs	0.75	[12]
Insulation	Ceramic	0.90	[11]
Bonding wire	Au	0.82	[11]

Table 4.1: Emissivity of the materials making up the laser and sub-mount

The emissivity value used to calibrate a thermal measurement also varies as a function of wavelength, humidity, angle of sample from the instrument, air pressure and the lens being used. All of these factors need to be taken into account in order to obtain the true temperature of any area in the image. In order to calibrate out all these factors from the measurements, it was assumed that at 0 mA of bias current every point in the image was at the heatsink temperature. Thus, by varying the heat sink temperature a calibration curve for each pixel in the image was obtained.

A picture of the experimental set-up is shown in figure 4.2. Due to the proximity of the camera to the laser, there was a concern that the laser radiation may damage the CCD chip. However, the lenses of the camera are made of germanium, which does not transmit [13] radiation at 1.3µm.

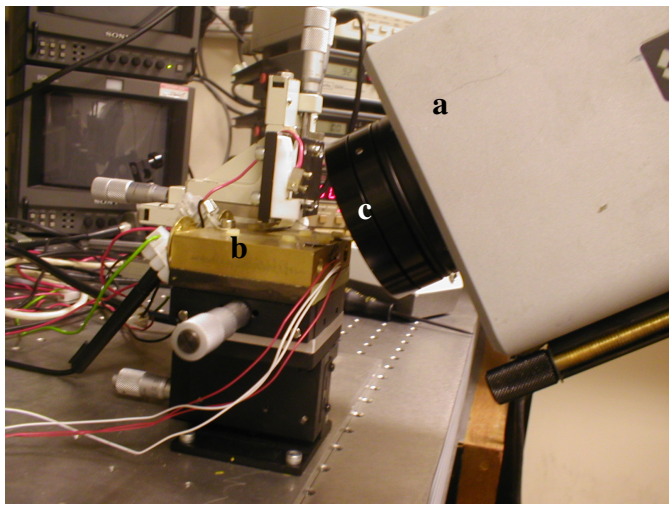

Figure 4.2: View of the thermal camera looking down on the laser diode which is mounted on a temperature stabilised block. a) Thermal camera, b) Temperature controlled stage, c) Germanium lens

4.3.2 Measurement procedure

The laser was first mounted on the temperature controlled stage with the front facet facing the camera. The camera was aligned and then focused on the laser. If the position of the camera relative to the laser changed during the measurement, it would invalidate the calibration and the measurement would have to be repeated. Thus, it was essential that the camera be clamped firmly in position. The heat sink temperature was then stabilised at the desired temperature (300K, 340K or 380K). The thermal camera was turned on and left to cool. Injection current was incremented in 5mA steps from 0mA until the beginning of roll-over and images were taken once the laser's temperature stabilised. The heat sink temperature was raised and the process repeated. When all three temperature measurements were finished, the laser was rotated so that the back facet could be imaged.

After all the images were taken, the data was post-processed using a C++ program, to obtain the true temperature values. A typical un-calibrated image obtained from this set of experiments is shown in figure 4.3.

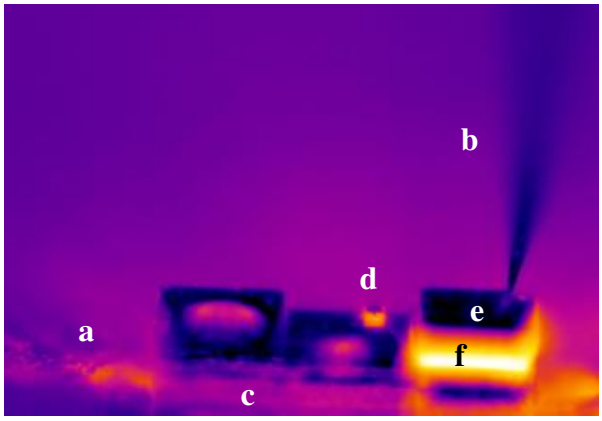

Figure 4.3: An uncalibrated false colour image of a laser and sub-mount taken at 380K with no bias current applied. a) heat sink, b) probe pin, c) sub-mount, d) laser, e) gold probe contact, f) ceramic block separating probe contact from sub-mount.

4.3.3 Data extraction

A typical calibrated image showing the true temperature of a 500µm long device is shown in figure 4.4. A zoomed in section of the image is shown in figure 4.5. The front facet and top contact can be made out, along with the wire bond.

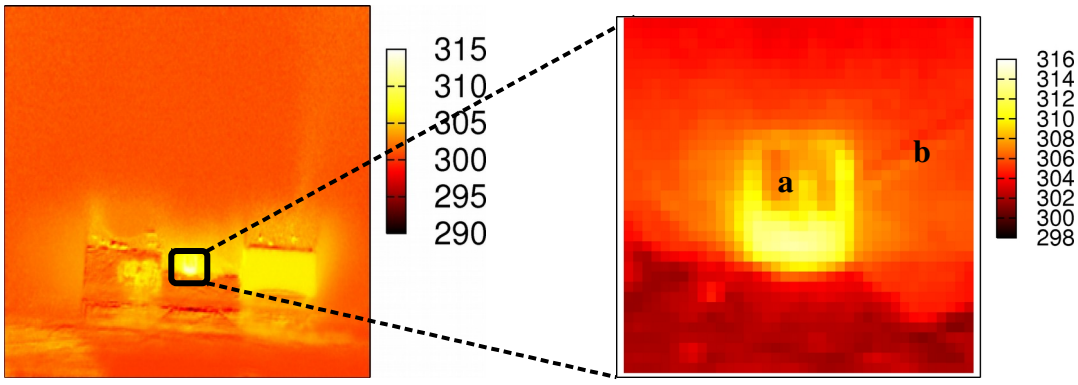

Figure 4.4: A typical thermal image taken of the laser and the sub-mount.

Figure 4.5: A magnified image of the thermal profile of laser (a). The bonding wire is just visible in the image (b).

Once the images were calibrated, data was extracted from the images as a function of current. Due to the large amount of data produced by these measurements, this process was automated with the use of a C++ program.

4.Error: Reference source not found3.4 Front facet, back facet and top contact temperature

To put the thermal measurements in perspective, the L-I curve of a coated 300μm device was measured. The same set-up as described above was used, but the thermal imaging camera was replaced with a broad area power meter (*Anritsu ML9001A* (instrument) and an *Anritsu MA7911A* (sensor)). Due to the high divergence of the laser radiation, not all of the light was collected. Thus, the L-I curves presented in this section do not contain all radiated power and are only relative. Figure 4.6 shows the L-I curves obtained at 300K, 340K and 380K. Figure 4.7 plots the corresponding rise in front facet temperature. It can be seen that the temperature increase of the front facet is surprisingly similar for all the heat sink temperatures. This suggests that the heat generation near the front facet depends only weakly on the heat sink temperature. Surprisingly there is no distinct change in the measured front facet temperature at threshold. One possible explanation for this could be that at these low power levels optical heating of the front facet plays a lesser role than carrier recombination heating at the front facet.

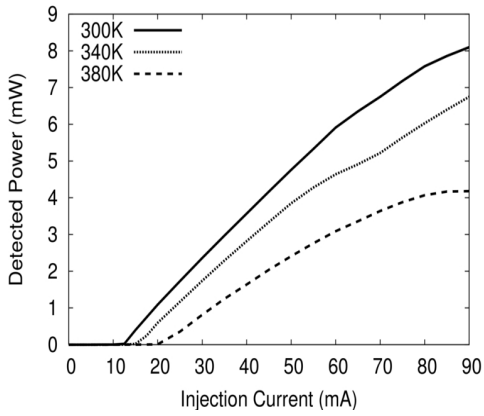

Figure 4.6: Typical L-I curves from the coated 300µm laser taken at 300K, 340K and 380K plotted against injection current.

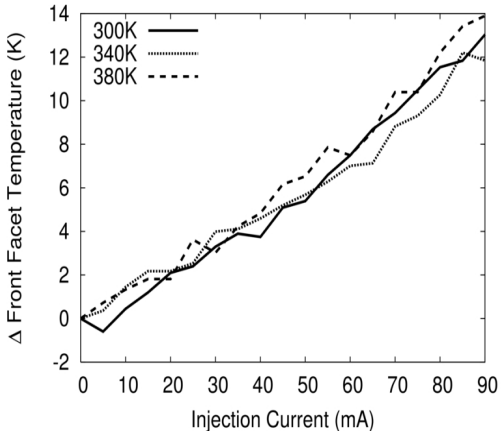

Figure 4.7: Extracted change in front facet temperature from the coated 300µm laser taken at 300K, 340K and 380K plotted against injection current.

The changes in front facet, back facet and top contact temperature for the 300µm coated device are plotted in figure 4.8. The increase in the top contact temperature is up to 10K less than that of the front facet. This is probably due to optical absorption and surface recombination on the front facet, making it the hottest part of the device. A further reason could be reduction of the top contact temperature due to heat loss to the air from the very large area of the top contact and heat conduction away from the device via the wire bond. Figure 4.9 is an image taken of the device in the visible spectrum. The wire bond is clearly visible and has a large surface area in contact with the top contact. It is entirely possible that a great deal of heat is being conducted up the wire and lost to the air, thus increasing the effective area (and cooling) of the top contact.

Figure 4.8 also shows that the back facet is cooler than the front facet by up to 2K. One possible reason for this could be the asymmetric top contact. If figure 4.9 is examined, it can be seen that at the back facet there is a wide coating of gold across the back of the laser. However, at the front where the chip identification numbers are etched into the GaAs, there is no gold. This could reduce the heat conduction away from the RW and increase the front facet temperature.

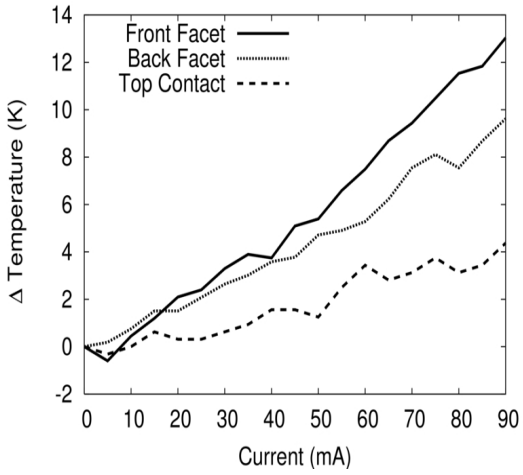

Figure 4.8: Front, back and top contact temperatures from the 300µm coated device.

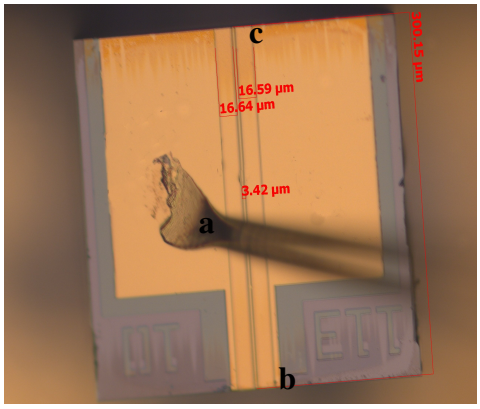

Figure 4.9: Image of the 300µm coated device, a) wire bond, b) front facet, c) back facet.

4.3.5 Device heating as a function of length

As shorter devices are more practical for high speed modulation, it is important to understand the impact of device length on self-heating. Figure 4.10 shows the front facet temperature of the coated (R_f=0.3, R_b=0.7), 300µm, 500µm and 750µm devices as a function of injection current. The general trend is that the longer the device, the

cooler it is, at a given injection current. The same trend can be seen in figure 4.11 for the uncoated cavities. In order to achieve threshold, a shorter device will need a higher carrier density than a longer device because more gain is required from a shorter cavity to overcome the same mirror loss. Due to the higher carrier density, SRH and Auger recombination will be higher. Thus, more heat will be generated within the cavity. In Chapter 3, the internal losses were shown to be carrier density independent, thus will not increase in shorter devices. Another reason for the shorter device being hotter is that it has a smaller volume, thus less heat (injection current) is needed to raise its temperature.

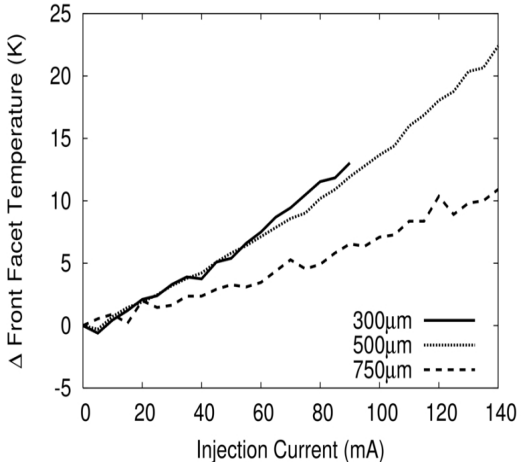

Figure 4.10: Front facet temperature of the 300µm, 500µm and 750µm coated devices as a function of length at 300K.

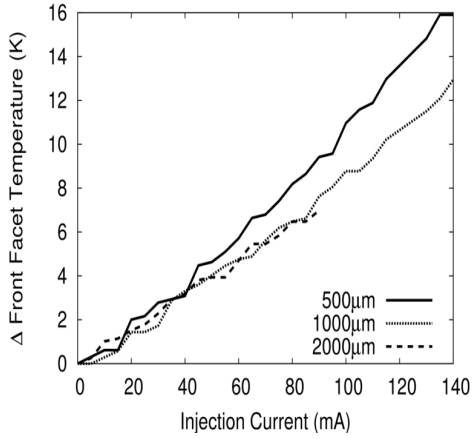

Figure 4.11: Front facet temperature of the 500µm, 1000µm device and 2000µm uncoated devices at 300K.

The front facet temperature for the coated and uncoated 500µm devices have been plotted in figure 4.12. At 140mA, the front facet temperature of the coated device

increases by 21K, while for the uncoated device it increases by 15K. One reason for this could be the higher photon density within the coated device, leading to higher free carrier absorption and thus heating.

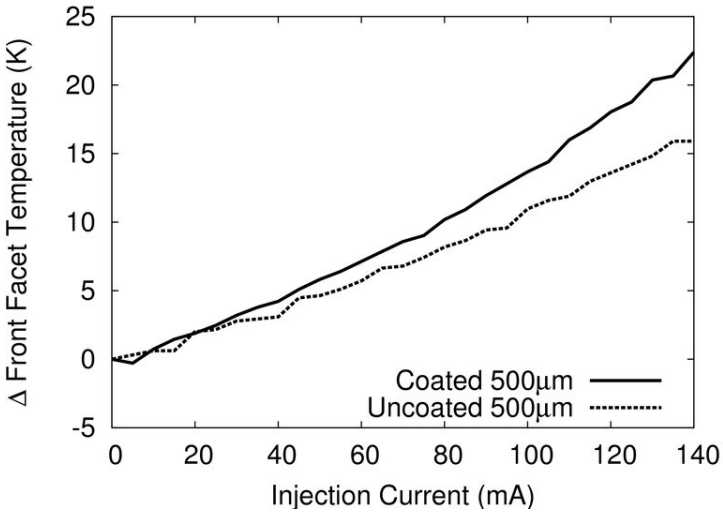

Figure 4.12: Front facet temperature of the coated and uncoated 500µm device compared.

4.3.6 Evidence for cooling through the bonding wire

Figure 4.13, shows three calibrated images of the 300µm coated device, the images are taken at three different heat sink temperatures all with 90mA of injection current. The calibrated images are plotted as an offset from the heat sink temperature. The bonding wire connecting the laser to the sub mount is visible as a faint line. This indicates that the bond wire is at a slightly elevated temperature and confirms that heat does indeed leave the device via the bonding wire. In figure 4.13b, evidence for heat leaving the device via convection can be seen as a halo of air of elevated temperature around the laser.

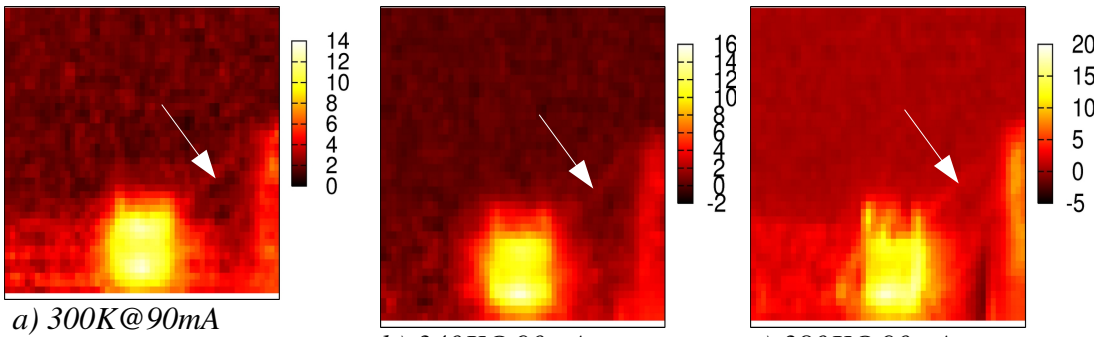

a) 300K@90mA *b) 340K@90mA* *c) 380K@90mA*

Figure 4.13: Three calibrated images of the 300µm laser. The wire bond can be seen in the images. These images are from the same view as shown in figure 4.3. These images are plotted as an offset from the heat sink temperature.

Figure 4.14 plots the temperature for a point on the wire indicated by the white arrows in figure 4.13. As the bias current is increased, the wire temperature also increases.

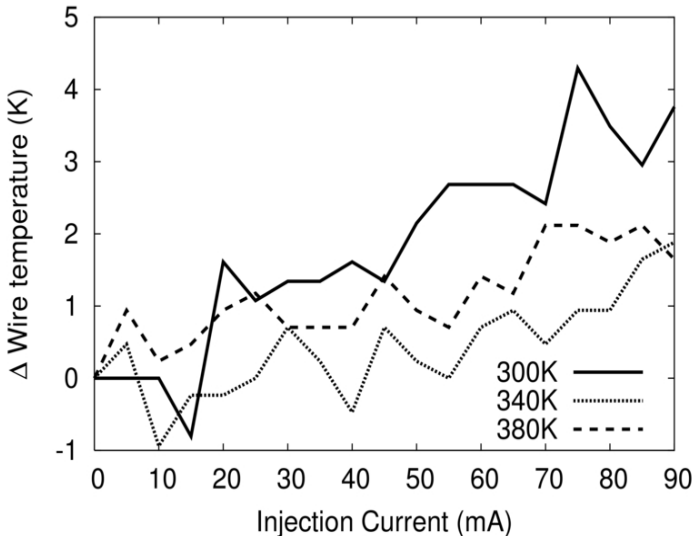

Figure 4.14: Heating of the wire at three different temperatures.

Joule heating within the wire can be eliminated as the source of heat with a simple calculation. The resistivity of gold is $\rho=2\times10^{-8}\,\Omega m$, the area of the wire is π x 25µm x

25μm and the length of the wire is approximately 300μm. The total resistance is given by.

$$R = \frac{\rho L}{A} \quad , \tag{4.1}$$

which results in R= $3.055 \times 10^{-3}\Omega$. At 90mA, the power dissipated in the wire is 24.75μW. Due to the highly conductive nature of gold, it is not possible to proceed using the specific heat capacity to calculate the increase in wire temperature. Instead, the heat propagation out of the wire must be modeled. This is achieved using the 1D heat equation,

$$\frac{\partial}{\partial x} k \frac{\partial}{\partial x} T + H = 0 \quad , \tag{4.2}$$

where T is the temperature, k the thermal conductivity and H is the heat source. Both ends of the wire are held at 300K, and the thermal conductivity of gold is taken as 317W $m^{-1}K^{-1}$, and equation 4.2 is solved using finite difference (FD) discretisation. The result of the FD calculation is plotted in figure 4.15. At the center of the wire a heat rise of only ~1.5mK was found - even though heat dissipation at the surface of the wire was neglected. This value is far below that of the measured temperature increase, suggesting that the elevated bond wire temperature is due to heat conduction away from the laser.

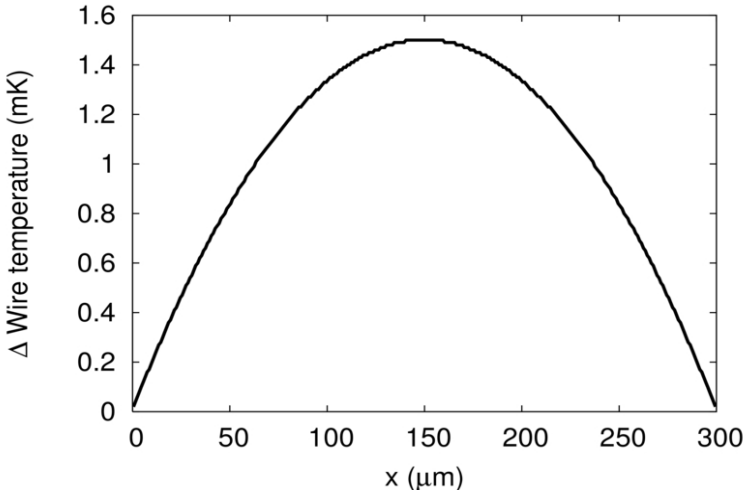

Figure 4.15: Thermal simulation of the wire

4.3.7 The transient thermal response of the laser

The transient thermal response of a laser is of use when performing any thermal measurement on a laser, be it photoluminescence measurements, reliability testing or thermal imaging, or to calibrate transient thermal simulations.

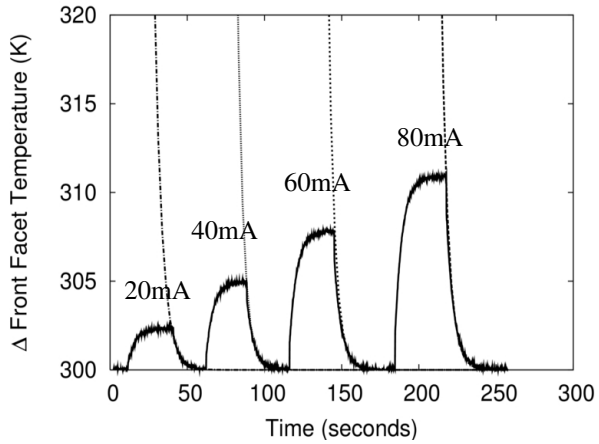

Figure 4.16: Recorded thermal response of laser at 300K for injection currents of 20mA, 40mA, 60mA and 80mA.

A slow pulse train was applied to the 750µm coated laser. A spot on the front facet

was chosen and the temperature monitored. Pulses of 20mA, 40mA, 60mA and 80mA were applied at each temperature. The results are plotted in figures 4.16, 4.17 and 4.18.

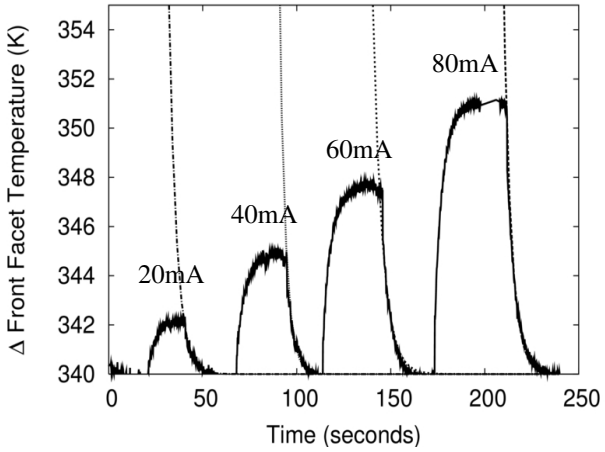

Figure 4.17: Recorded thermal response of laser at 340K for injection currents of 20mA, 40mA, 60mA and 80mA.

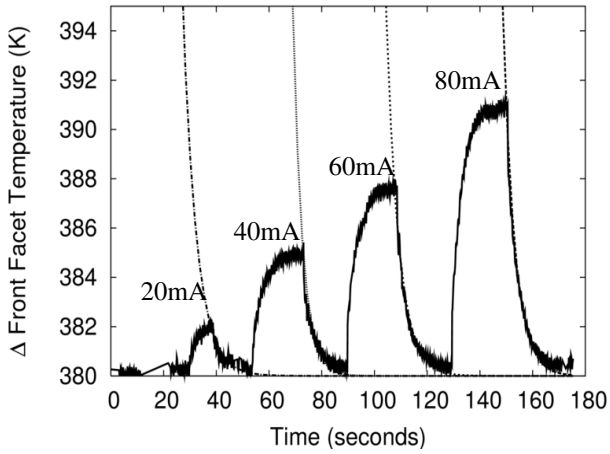

Figure 4.18: Recorded thermal response of laser at 380K for injection currents of 20mA,40mA, 60mA and 80mA.

The cooling of a body is described by Newton's law of cooling

$$\frac{dT}{dt} = -k(T - T_{amb}) \quad , \tag{4.3}$$

where T_{amb} is the ambient temperature, $T(0)$ is the temperature of the laser when the pulse is turned off and k is a positive constant determined from fitting. The solution to the ordinary differential equation is

$$T(t) = T_{amb} + (T(0) - T_{amb})e^{-kt} \quad . \tag{4.4}$$

In order to quantify the speed of cooling of the laser, equation 4.4 was fit to the above cooling curves and k was extracted. The values obtained for k are plotted in table 4.2. The average cooling constant is $0.24 s^{-1}$ and was found not to be a function of temperature or injection current.

	20mA	40mA	60mA	80mA	Average (s^{-1})
300K	0.2	0.25	0.24	0.23	0.23
340K	0.24	0.3	0.2	0.25	0.25
380K	0.19	0.28	0.21	0.23	0.23

Table 4.2: Cooling constants.

4.4 Limitations of direct thermal imaging

Due to the long wavelength IR radiation used in direct thermal imaging, measurements are usually limited by the spatial resolution of the lens according to the Rayleigh limit

$$x_{min} = f\left(\frac{1.22\lambda}{D}\right) \quad [14], \tag{4.5}$$

where D is the lens diameter, f is the focal length and λ is the measurement wavelength. The spatial resolution of the Flir SC3000 camera and microscopic lens is ~30µm. This is acceptable for looking at large regions (e.g. substrate and top contact). However, another technique must be found if a detailed thermal profile of the laser structure is to be resolved. This becomes clear if figure 4.19 is examined, where a simulated thermal profile of the laser epitaxy and the substrate is plotted and the high temperature laser structure can seen. However, when a 30µm x 30µm averaging window is applied, the very high temperature of the QW is averaged out. In the next section, the thermally induced changes in lasing wavelength are used to gain a better understanding of the active region temperature.

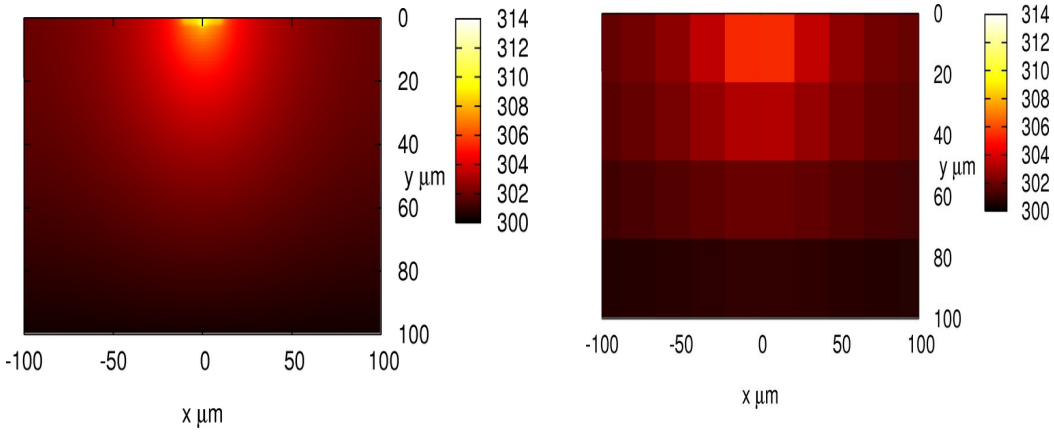

Figure 4.19: a). A thermal simulation of a 1.3µm dilute nitride edge-emitting laser b.) Pixelation of the image due to the large spatial resolution of the thermal imaging camera.

4.5 Spectral measurements

4.5.1 Active region temperature

The temperature of the active region is of particular interest as far as device operation and lifetime are concerned. As the device temperature is increased, the QW band gap shrinks and thus the lasing wavelength red shifts. If the wavelength can be corresponded to a temperature, a weighted average of the active region temperature can be estimated. The red shift with temperature can clearly be seen in the above threshold spectra shown in figure 4.20.

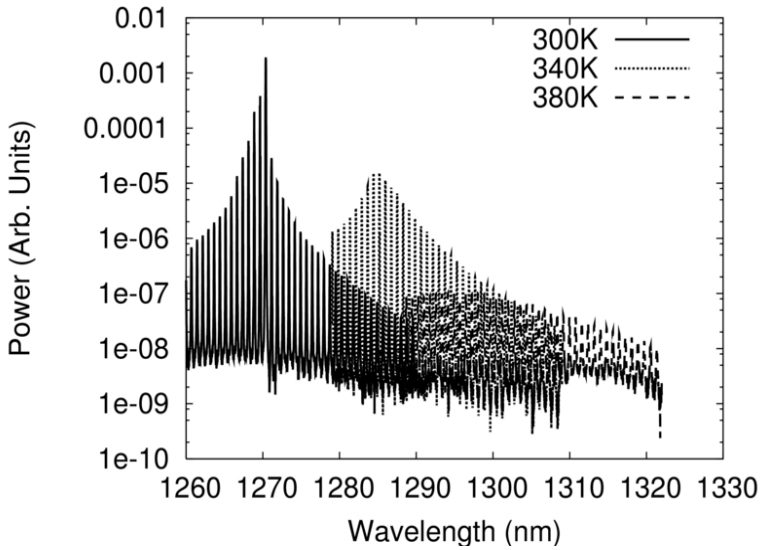

Figure 4.20: Lasing wavelength shift of a 300μm device operating at 15mA.

In the final part of this chapter, the temperature dependent shift of the lasing spectra is measured to estimate the QW temperature. This is done using the same experimental system as described in Chapter 3. Instead of just running the laser below threshold (as

in Chapter 3), the laser was run from far below threshold up until the recommended operating limit of the device. The spectra were captured, the peak lasing wavelength extracted and the weighted average of the QW temperature is estimated.

4.5.2 Results

Figure 4.21 plots the peak lasing wavelength of the lasing spectra for the 300μm device as a function of injection current and temperature. Below threshold, a blue shift in the lasing wavelength is observed as the injection current is increased. This blue shift is due to band filling. At threshold (~20mA), the carrier concentration clamps and no further blue shift is observed in the spectra. At this point, band gap shrinkage due to heating effects starts to dominate. If it is assumed that the above and below threshold heating mechanisms are the same, the impact of the blue shift on the lasing wavelength can be removed by extrapolating the above threshold peak lasing wavelengths back to 0mA. The black lines in figure 4.21 show this extrapolation. At 0mA there is no self heating. A graph of "peak lasing wavelength" at 0mA versus active region temperature can be plotted as shown in figure 4.22.

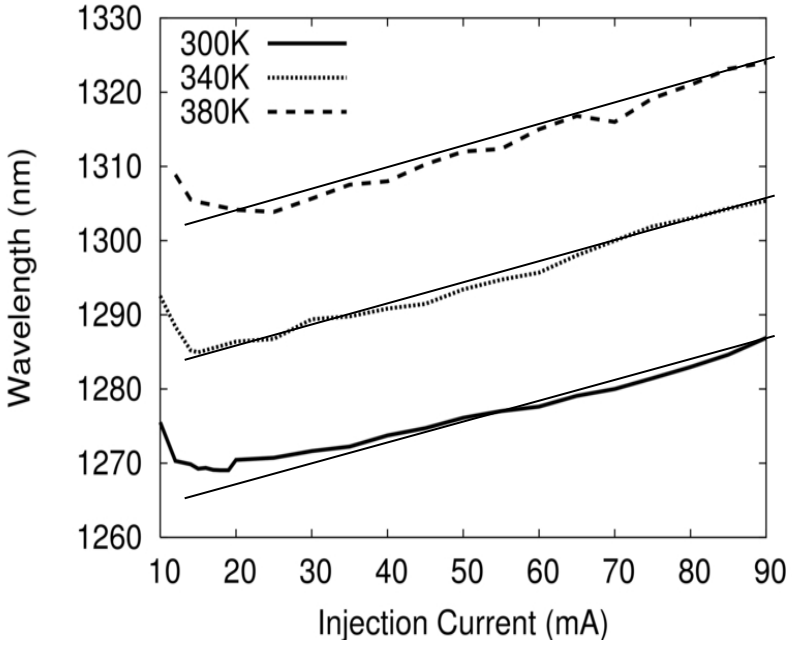

Figure 4.21: Lasing wavelength as a function of injection current and heat sink temperature.

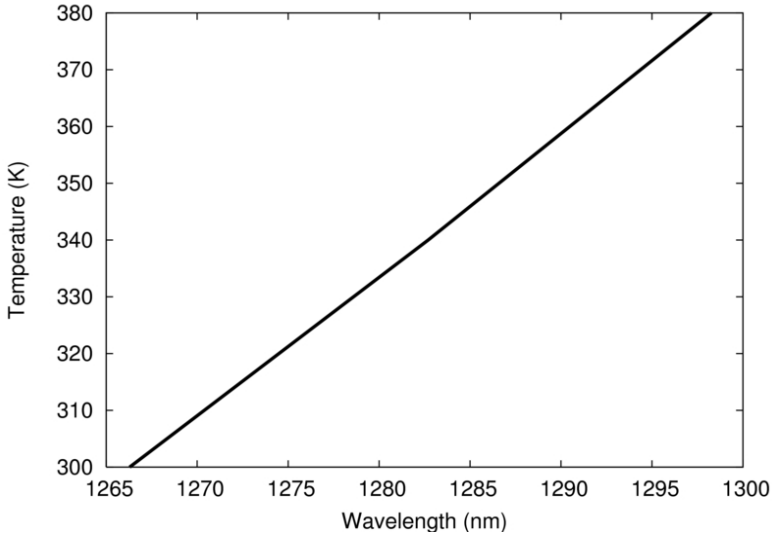

Figure 4.22: Calibration curve converting wavelength to temperature.

Figure 4.22 can then be used to convert the measured above threshold lasing wavelengths into estimated QW temperatures. Figure 4.23 plots the estimated increase in QW temperature versus injection current. At higher heat sink temperatures, self heating raises the QW temperature more than it does at low heat sink temperatures because of the increased Joule heating due to a lower mobility, higher Auger recombination rates, higher carrier escape rates and higher free carrier absorption. At 90mA, a 7.5K rise in QW temperature due to increased self heating is observed for every 40K rise in heat sink temperature .

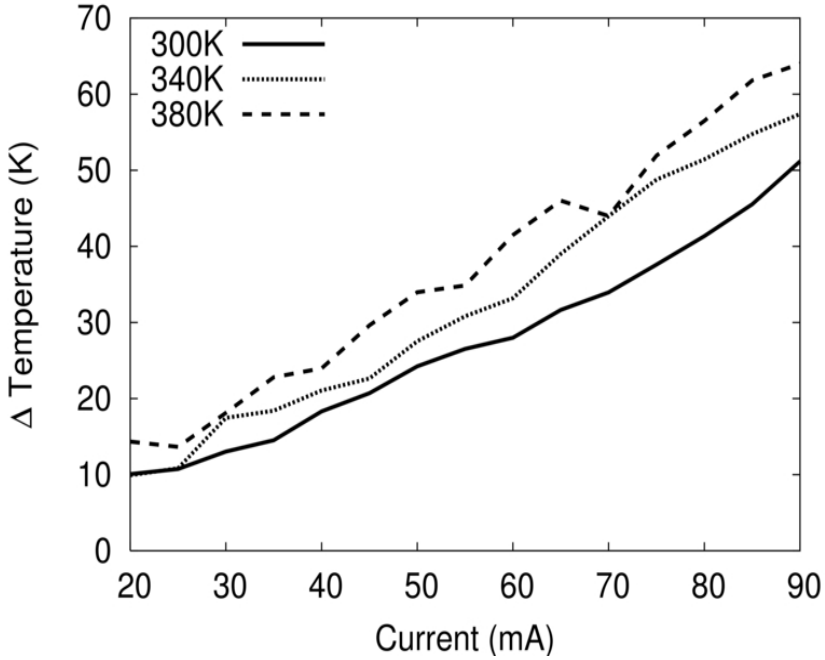

Figure 4.23: Estimated shifts in QW temperature.

4.5.3 Error in estimation of QW temperature

Above threshold, the thermally induced band gap shrinkage is known to dominate

wavelength shift. There are however other effects (band-gap re-normalisation and band filling) which also contribute to the change in lasing wavelength. In order to estimate the error in the active region temperature, it is essential to know by how much the change in wavelength is being effected by these other effects. In this section, our calibrated in-house 2D electro-optical-thermal simulation tool is used to estimate this error.

4.5.3.1 Red shift due to band-gap re-normalisation

As carriers are injected into the QW, the band gap shrinks due to increased Coulomb screening. This can be expressed by

$$dE_g = -2.2\text{x}10^{-6} \cdot L \cdot \left(\frac{n+p}{2}\right)^{0.34} \quad [15], \tag{4.6}$$

where dE_g is the amount the band gap shrinks, L is the QW width and n,p are the carrier densities (m^{-3}).

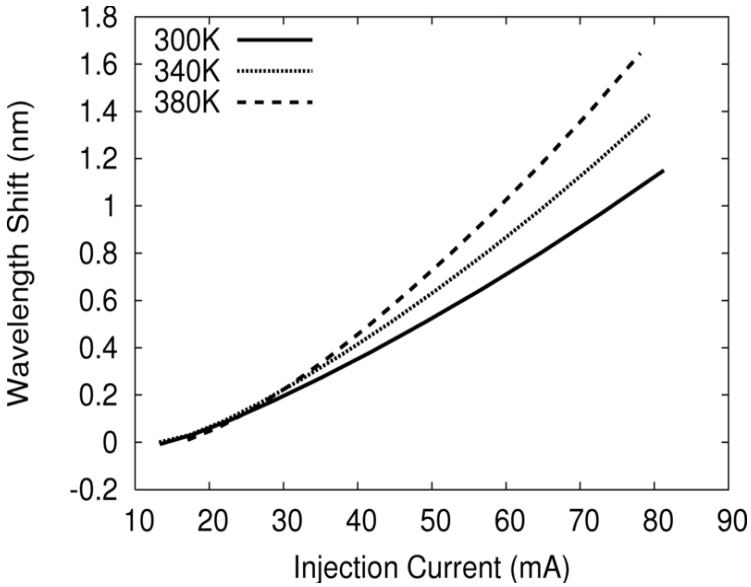

Figure 4.24: Red shift due to band gap re-normalisation.

Our calibrated opto-electro-thermal device simulator was run above threshold and dE_g calculated from equation 4.6. Figure 4.24 shows the result of this calculation, expressed in terms of shift in wavelength.

4.5.3.2 Blue shift with increased carrier density – Band filling

As the number of carriers in the QW increases, the average lasing energy also increases. This causes a blue shift in the gain and the lasing emission (see figure 3.15). Using our in house calibrated gain simulation tool, a linear fit to the blue shift of the peak lasing wavelength as a function of carrier density was performed. The expression

$$dE_g = C \cdot \frac{(n+p)}{2} \tag{4.7}$$

with C =-17x10^{-24} was obtained to approximately describe the blue shift of the lasing wavelength with carrier density.

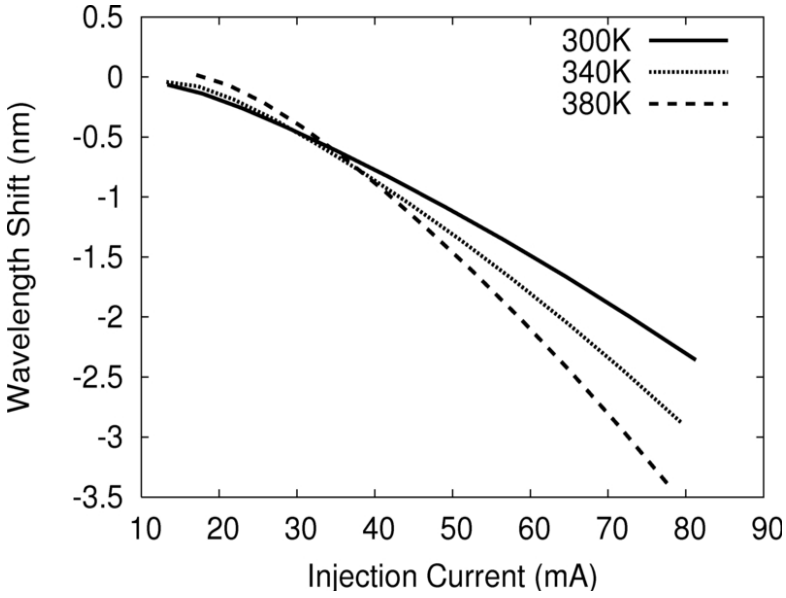

Figure 4.25: Simulated blue shift due to increased electron density.

Again, our in-house optoelectronic simulation tool was run to obtain the QW carrier density as a function of injection current. The simulated carrier density was then used in equation 4.7 to estimate the blue shift. The result is plotted in figure 4.25.

4.5.3.3 A combination of the effects

Figure 4.26 plots the impact of the shift due to band gap re-normalisation and band filling. It can be seen that the net wavelength shift due to both of these effects is negative (blue shift). Therefore, if these effects are not accounted for, the thermally-induced red shift will be underestimated and thus so will the temperature.

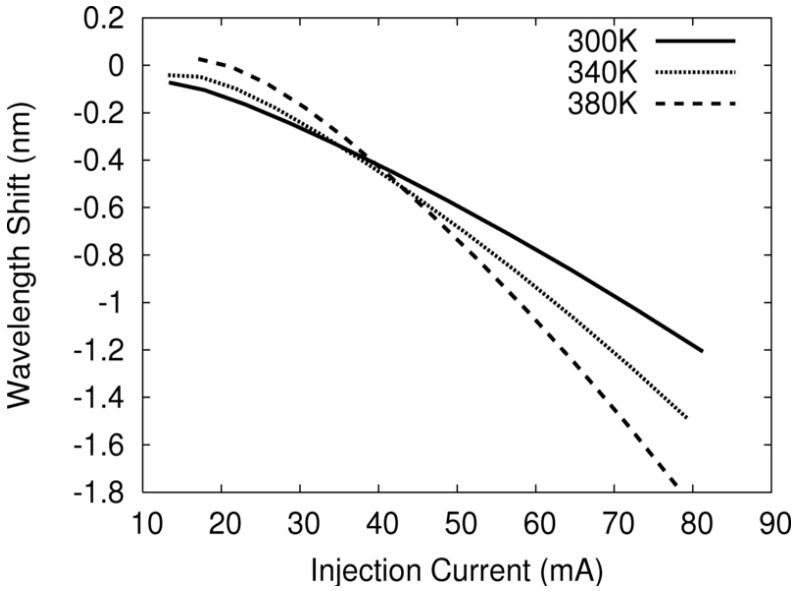

Figure 4.26: Combination of blue shift and band gap re-normalisation shift is small

The results suggest that the temperature in figure 4.23 could be underestimated by up to 5K. It should also be noted that the temperature will vary along the cavity as a function of photon density. Thus, the temperature presented in figure 4.23 represents the device temperature averaged along the cavity and not the maximum temperature

present within the device.

4.6 Summary

Thermal imaging at 8μm has been found to be a useful tool to gain understanding of the thermal performance of the top contact and facets. The top contact has been found to heat up less than the facets, while the front facet has been found to be hotter than the back facet. The front facet temperature of the 500μm coated devices was higher than that of the uncoated devices. This may be possibly due to the higher photon densities within the device.

A temperature rise of a few degrees was observed in the gold bonding wire as injection current was increased. Using finite difference simulation, it was shown that this is not due to self-heating. Consequently, the bonding wire has been identified as a major heat conduction path away from the top contact and ridge. Measurements of the thermal transient response of the device have been made and a cooling constant of k=0.24s^{-1} was extracted. k was found to independent of both temperature and injection current.

Thermal imaging suggested a low level of self heating within the device. However, due to the limited spatial resolution of the camera, this had to be verified with another technique. The QW temperature was estimated by measuring the lasing wavelength as a function of injection current and temperature. At 380K with 90mA of injection current, the active region was found to be 60K hotter than the heatsink temperature.

This corresponds to a true operating temperature of ~440K. However, simulations suggest that this temperature is underestimated by up to 5K.

4.7 Further work – improvements to the measurement system

If more time and funding were available, the following improvements to the measurement system would be made:

1. The thermal camera measurement system would be automated as the gain measurement setup was. This was not done during the course of this work because the camera was only on loan to us for a month.
2. A thermal camera with a lower wavelength range 3-5μm [5] would give more detailed temperature profiles.
3. Raman spectroscopy or micro-photomodulated photoreflectance could be used in conjunction with thermal imaging. This would enable a more accurate picture of facet temperature profile to be generated. It would also reduce our reliance upon measurements of the lasing spectra.
4. If spectral measurements were to be performed again, they would be done with a pulsed power supply. This would enable the true lasing wavelength to be determined without lattice heating. Thus, the QW temperature would be obtained more accurately [17].
5. The camera would be bolted to the optical bench to eliminate any possibility the camera moving during the measurement process.

4.8 References

[1] A. Kozlowska, J. W. Tomm, P. Wawrzyniak, A. Malag, F. Weik and M. Latoszek, "Studies of the degradation mechanisms in high-power diode lasers using multi-channel micro-thermography", Proceedings of SPIE, 5958, pp. 223-229, 2005

[2] A. Kozlowska and P. Wawrzyniak, J. W. Tomm, F. Weik, and T. Elsaesser, Appl. Phys. Lett. 87, 153503, "Deep level emission from high-power diode laser bars detected by multispectral infrared imaging", 2005

[3] T. Tien, F. Weik, Jens W. Tomm,B. Sumpf, M. Zorn, U. Zeimer, and G. Erbert "Thermal properties and degradation behaviour of red-emitting high-power diode lasers", Appl. Phys. Lett., 89, 181112, 2006

[4] A. Kozlowska, P. Wawrzyniak, A. Malag, M. Teodorczyk,J. W. Tomm and F. Weik, "Reliability screening of diode lasers by multispectral infrared imaging", J. Appl. Phys. 99, 053101, 2006

[5] A. Kozlowska, M. Latoszek, J. Tomm, F. Weik, T. Elsaesser, B. Spellenberg and M. Bassler, "Analysis of thermal images from diode lasers: Temperature profiling and reliability screening ", App. Phys. Lett., 86, 203503, 2005

[6] S. Todoroki, "Influence of local heating on current-optical output power characteristics in Ga1−xAlxAs lasers" ,J. Appl. Phys. , 60, p.61, 1986

[7] S. Sweeney, L. Lyons, A.. Adams, and D. Lock "Direct Measurement of Facet Temperature up to Melting Point and COD in High-Power 980-nm Semiconductor

Diode Lasers" IEEE J. Sel. Topitcs in Quant. Electron., 9, 5, p.1325, 2003

[8] P.-W. Epperlein, "Micro-Temperature Measurements on Semiconductor Laser Mirrors by Reflectance Modulation: A Newly Developed Technique for Laser Characterization",Jpn. J. Appl. Phys., 32, pp. 5514-5522, 1993

[9] A. R. Adams, E. Cariou, P. Vicente, B. Couzinet, and A. Raymond, Proc. 7th Eur. Conf. Integrated Optics (ECIO'95), pp.121–124, 1995

[10] R. Puchert, A. Bärwolff, M. Voß, U. Menzel, J. W. Tomm, and J. Luft," Transient thermal behavior of high power diode laser arrays", IEEE Trans. Compon. Packag. Technol. 23, 1, pp. 95-100, 2000

[11] Electro Optical Industries, "Material Emissivity Properties", http://www.electro-optical.com/ bb_rad/ emissivity/ matlemisivty.htm, accessed Jan 24th 2008

[12] R. Houdrt, C. Hermann and G . Lampel "Photoemission and Photoluminescence from GaAs/GaAIAs Superlattices Physica Scripta", Vol. T13, pp. 241-244, 1986

[13] Infrared Multi Layer Laboratory, The University of Reading. http://www.irfilters.reading.ac.uk/ library/technical_data/infrared_materials/ge1.htm accessed Jan 24th 2008

[14] S. Bull, "Photo- and Electroluminescence Microscopy and Spectroscopy Investigations of High Power and High Brightness Semiconductor Laser Diodes", PhD Thesis University of Nottingham September 2004

[15] A. Schonfelder, J.D. Ralston,K. Czotscher, S. Weisser, and J. Rosenzweig and E.C. Larkins “Optical gain and spontaneous emission in InGaAs/GaAs multiple quantum well laser diodes”, J. Appl. Phys., 80, 1, pp.582-584 ,1996

[16] Private communication J.J.Lim Univeristy of Nottingham 2007

[17] Bernt Witzigman NUSOD 2007. Private communication